Producing and imaging quantum turbulence via pair-breaking in superfluid ^{3}He-B

M. T. Noble, S. L. Ahlstrom, D. I. Bradley, E. A. Guise, R. P. Haley, S. Kafanov,
G. R. Pickett, M. Poole, R. Schanen, T. Wilcox, A. J. Woods, D. E. Zmeev, and V. Tsepelin*
Department of Physics, Lancaster University, Lancaster, LA1 4YB, UK
(Dated: March 15, 2022)

Destroying superfluidity is a fundamental process and in fermionic superfluid such as ^{3}He-B it splits Cooper pairs into thermal excitations, quasiparticles. At the lowest temperatures, a gas of these quasiparticle excitations is tenuous enough for the propagation to be ballistic. We describe here an exploitation of the ballistic quasiparticles as the "photons" to observe the local destruction of superfluid ^{3}He-B by a mechanical resonator. We use a 5 by 5 pixel quasiparticle camera to image an emergence of quasiparticle excitations and a tangle of quantized vortices accompanying the pair-breaking. The detected quantum tangle is asymmetric around the mechanical resonator and is governed by the stability of vortices on the resonator surface. The vortex distribution shows that a conventional production of a quantum tangle via repetitive emission of vortex rings starts on the top surface of the generator and spreads around whole surface at high velocity when escaping vortex rings get re-trapped by the moving resonator.

Superfluid flow is dissipationless only below the Landau critical velocity, while at higher velocities it becomes energetically favourable to break-up the condensate and to produce elementary excitations [1]. Recently there have been a number of observations and theoretical works showcasing the exceeding of the Landau velocity [2–4], including superfluid ^{3}He discussed here. The Cooper pairs in superfluid ^{3}He, being p-wave paired, have non-zero spin and orbital angular momenta, leading to a complex 18-component order parameter [5–7]. As a result of this complexity, the details of pair-breaking are still under debate [3, 8–11]. Furthermore, the pair-breaking process is accompanied by production of quantised vortices, one of many topological effects supported in superfluid ^{3}He [7, 12–18].

In the limit of zero temperature, quantised vortices form a dynamic disordered tangle, which is known as pure superfluid turbulence [19]. Superfluid vortex tangles are produced via the interaction of independent vortex rings emitted by an oscillating structure [17, 20] or via multiplication of vortex lines near a boundary in the presence of superfluid flow [21]. Ultimately, an expansion of a Kelvin-wave loop on a trapped vortex line governs both processes. An applied superfluid flow buckles the vortex line pinned to a surface, the vortex develops and grows a Kelvin-wave loop until it reconnects with itself. The self-reconnection results in the "vortex mill" [20, 22, 23], repetitive generation of vortex rings which at a critical density will form a tangle. If the expanding loop instead reconnects with a boundary it produces further Kelvin-waves loops on a newly attached vortex segment, repeating the process [21], also resulting in a tangle.

While we understand conceptually how a tangle should develop and numerical simulations show the process [24, 25], the experimental data demonstrating the development is sparse and mostly based on the time of the flight of the vortex rings [17, 26, 27]. We know that rings form a tangle, but it is nearly impossible to probe the spatial distribution of vortices in a quantum tangle around a turbulent source due to the small size of the vortex core. Here we utilise unique property of broken Cooper-pairs (quasiparticles) to experience Andreev reflection at an energy barrier [28, 29] and map out quantum turbulence surrounding a vibrating wire resonator. We "illuminate" a vortex tangle by the quasiparticle excitations ("photons") in the superfluid itself and measure the shadow of created turbulence during pair-breaking, which allows us to look at mechanisms behind the tangle formation.

I. EXPERIMENTAL SETUP

The left panel of Fig. 1 shows the innermost part of our experimental setup where all of the components are submerged in superfluid ^{3}He-B below 150 µK. The generator vibrating wire resonator (VWR) that can controllably destroy the superfluidity and create quantum turbulence is located in the center of the cell. To visualize the products of the pair-breaking process, we utilise the quasiparticle blackbody radiator (BBR) [10], a device which can both produce and detect ballistic quasiparticles in superfluid ^{3}He. The BBR consists of an enclosure with an orifice, a heater VWR (Q_{BBR}), which when operated above the pair-breaking velocity, will generate excitations and a thermometer VWR (T_{BBR}) to detect quasiparticle excitations. A BBR can operate either in a "furnace" mode as a thermal quasiparticle source or as a bolometer to detect ambient and incoming quasiparticles [10]. The BBR is located 1 mm away from the generator VWR and has its orifice aligned with the apex of the generator wire. On the other side of the generator the cell has the quasiparticle camera [30], a 5×5 array of mini-BBR detectors. Each camera pixel consists of a 1 mm diameter cylindrical cavity in the copper block with a miniature quartz tuning fork resonator inside acting in the same way as a thermometer VWR but on a smaller scale. The cell

* v.tsepelin@lancaster.ac.uk

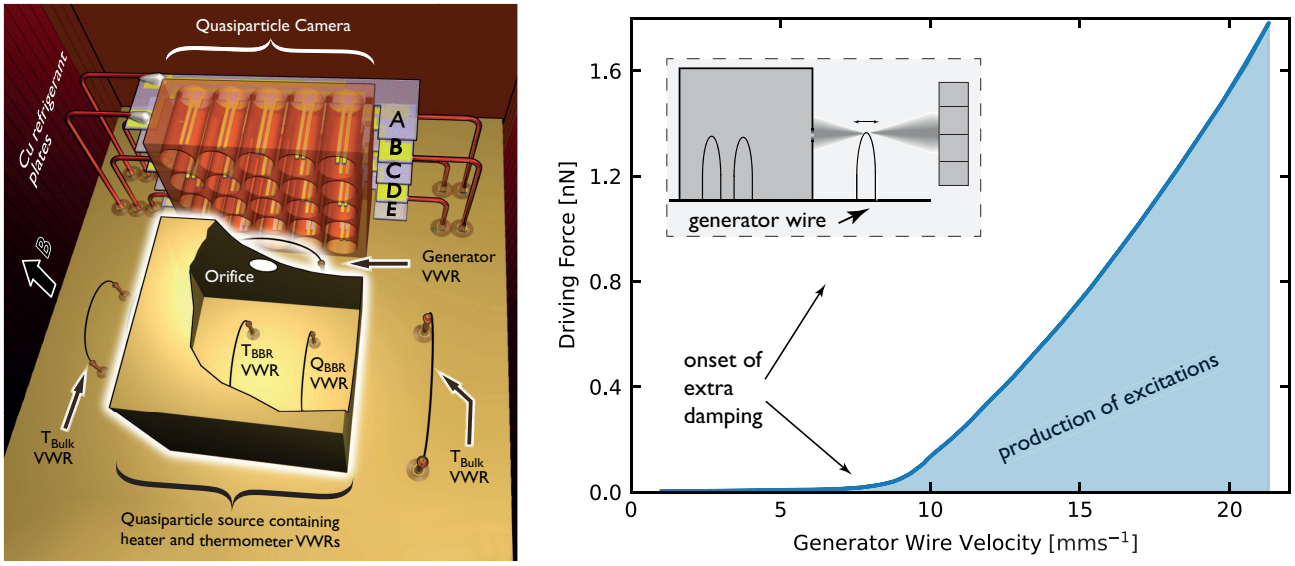

FIG. 1. (*Left*) A sketch of the experimental cell used to controllably destroy the superfluidity and image an accompanying quantum vortex tangle. The quasiparticle source (blackbody radiator, BBR) illuminates a turbulent tangle created by the generator wire in front of a quasiparticle camera. The BBR consists of a box, containing two vibrating wires to generate (heater, Q_{BBR}) and detect (thermometer, T_{BBR}) excitations [10]. Excitations produced within the box quickly thermalise and emerge from a small hole (the radiator orifice), forming a wide beam of ballistic excitations. The beam propagates towards the quasiparticle camera [30], which is placed 2 mm away from the radiator's orifice and has a 5×5 array of pixels. Each pixel in the camera consists of a 1 mm diameter cylindrical cavity in a copper matrix with a miniature quartz tuning fork resonator inside that detects incident quasiparticles. The turbulent tangle reduces number the quasiparticles reaching the camera and forms a shadowgram. (*Right*) The force velocity dependence of the generator wire. The onset velocity for excitation production is highlighted by an arrow. The inset depicts emission of a quasiparticle beam by the generator wire above the onset velocity.

contains several other vibrating wires that detect ambient quasiparticles and are used as thermometers. For the cooling methods and operating principles of a BBR we refer the interested reader to the Materials and Methods section.

II. RESULTS

The right panel of Fig. 1 shows the measured force-velocity dependence of the generator wire. At low velocities the generator has a minute damping and the motion of the wire only scatters ambient quasiparticles present in the superfluid. Above approximately 7.5 mm s^{-1} the wire damping rapidly increases due to the creation of excitations. The force-velocity dependence contains no information about what kind of excitations are created, it merely demonstrates the onset of power loss into the surrounding superfluid. First, we will demonstrate that the generator wire, which exceeds the pair-breaking velocity, emits a beam of quasiparticle excitations. Second, we will characterise a beam of quasiparticles emitted by BBR in a "furnace" mode and contrast it with the generator wire beam. Finally, we will use the BBR beam to "illuminate" the generator wire breaking superfluid and observe the distribution of quantum vortices surrounding the generator.

A. Quasiparticles Emitted by the Generator Wire

The largest fractional increase of dissipation in Fig. 1 occurs at $\sim 9\,\mathrm{mm\,s^{-1}}$, around a third of the Landau critical velocity ($v_L = 28\,\mathrm{mm\,s^{-1}}$ at 0 bar [6]), which we attribute to pair-breaking expected for an oscillating object in superfluid ^{3}He-B [11]. At this velocity quasiparticles near the wire surface can escape into the bulk superfluid due to the enhancement of superfluid flow around a cylindrical shape of the wire [11]. The escaped quasiparticles travel ballistically away and scatter with the cell walls and surrounding detectors. The quasiparticle camera positioned in front of the generator VWR detects the excitations traveling towards it and acquires "images" of the quasiparticle flux incident on its pixels. In our temperature range the measured quasiparticle flux is directly related to the detected power [10] and we will use both terms in the manuscript (for the details of the detector operation and their calibration see the Materials and Methods section).

Figure 2 summarises the measurements of quasiparticles emitted by the generator wire towards the camera as a function of wire velocity. The left panel of the figure presents the camera "images" at four selected velocities plotted as a Hinton-based diagram. It is clear that the central pixels are the first to detect the emission of excitations in agreement with the onset of damping taking place on the apex of the generator wire as the wire is

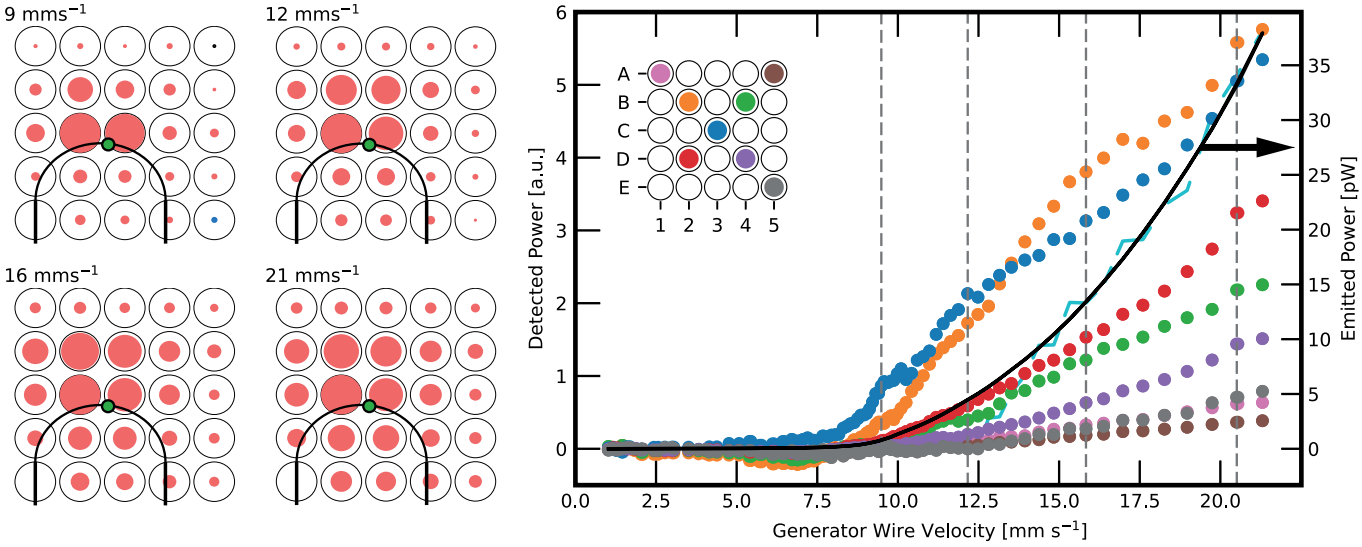

FIG. 2. Measurements of quasiparticle beam produced by the generator wire. *(Left)* Hinton-based diagrams of the detected quasiparticle flux for four generator wire velocities that are marked on the right panel as the dashed vertical lines. At 9 mm s^{-1} the measured beam is narrowest and broadens as the velocity of the generator wire increases. Each diagram is normalised by the largest flux measured at the given velocity. The radius of a circle corresponds to the value of the flux measured by the pixel. The green circle shows the scaled size and location of the BBR orifice. *(Right)* The dependence of the detected power carried by incoming quasiparticles for the diagonal pixels of the camera as a function of the generator wire's velocity. The non-diagonal pixels were measured but omitted from the figure for clarity. They are, however, included in the left panel images. The central pixels of the camera detect a quasiparticle beam when the generator velocity reaches approximately 7.5 mm s^{-1}, while the peripheral pixels detect the change at higher velocities. The solid black line shows the power $P = Fv$ emitted by the generator wire which we can measure directly. The power detected by each pixel can only be inferred, which is why the data points are presented in arbitrary units. However, if we sum this quantity over each pixel we get the dashed cyan curve, which is directly proportional within the noise to the total emitted power.

accelerating. The "images" demonstrate that the quasiparticle beam broadens with the increasing wire velocity. At the lowest velocity the emitted beam profile is slightly wider in the horizontal direction (along the wire's length), which reflects semicircular shape of the generator wire loop with a leg spacing of 3.2 mm.

The right panel shows the detected power by the camera's diagonal pixels as the velocity of the generator wire increases from 1 mm s^{-1} to 21 mm s^{-1}. The appearance of a flux of quasiparticles below 9 mm s^{-1} is in good agreement with the force-velocity curve in Fig 1. Comparison of gradients of the power emitted by the BBR and detected by individual pixels also shows that the beam becomes wider and more uniform at higher velocities.

The quasiparticles travel ballistically away from the pair-breaking point-source in a conical beam [10]. The cone's angle θ widens with the velocity v of the wire as [11]:

$$\cos(\theta) = \frac{\Delta}{p_F v} - \alpha, \tag{1}$$

where Δ is the superfluid gap energy, p_F is the Fermi momentum and α is the enhancement of the superfluid velocity by the wire. At the critical velocity on the cusp of quasiparticle production the angle of emittance is zero and allows us to determine α. For a perfect cylinder α should equal 2, while for a generator wire the asperities on its surface increase the superflow locally and we find $\alpha = 2.64$. The function of the angle θ is steep and after a velocity of 9 mm s^{-1} to 10 mm s^{-1} all camera pixels detect the emitted quasiparticles in agreement with the data.

B. Quasiparticles Emitted by the BBR Quasiparticle Source

Before revealing the distribution of turbulence around the generator wire we present the profile of quasiparticle beam emitted by the quasiparticle source employed to "illuminate" the tangle and cast shadows on the camera. In the "furnace" mode, the BBR heater wire is driven above the critical velocity (≈9 mm s^{-1} at 0 bar) similarly to the generator wire and its motion breaks Cooper pairs in the condensate [10, 11, 31]. In contrast to the generator wire where excitations can directly escape to the bulk liquid, the quasiparticles created in the BBR are confined within the box, rapidly thermalise and emerge as a beam of ballistic excitations from a 0.3 mm diameter hole (the radiator orifice). The thermometer wire in the BBR shows when the equilibrium conditions are reached: i.e. the temperature becomes stable. According to thermodynamics in the steady state all the power deposited in the BBR escapes away through the orifice towards the

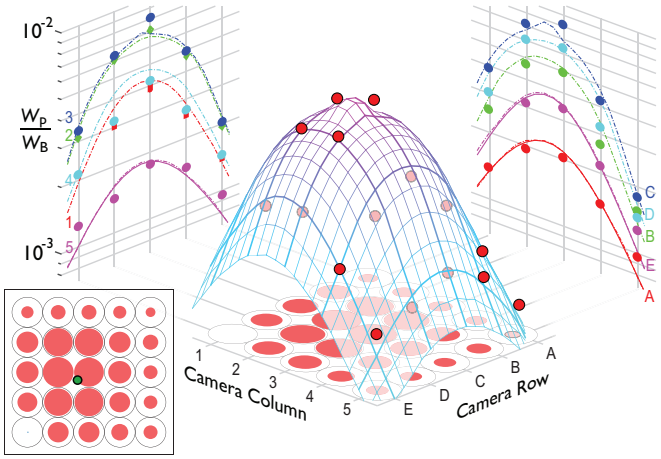

FIG. 3. The blackbody radiator's beam as the ratio of detected and emitted quasiparticle flux. The solid lines correspond to an analytical model of the quasiparticle emission. The dashed lines and mesh shows a numerical simulation of quasiparticle beam behavior (see text).

camera as a beam of quasiparticles.

The inset of Fig. 3 shows an "image" of the quasiparticle beam emitted by the BBR at an applied power of 800 pW. At this power the temperature inside the BBR reaches 262 µK while the surrounding bulk superfluid is at 135 µK. The image demonstrates that the beam is nearly symmetric and is slightly offset (0.5 mm vertically and 0.3 mm horizontally) with respect to the centre of the camera due to the imperfect alignment of the BBR orifice and the camera. The signal measured by the central pixels is nearly an order of magnitude larger than that by the peripheral pixels.

The angular dependence of the quasiparticle flux arriving at a camera pixel p with respect to the normal of the BBR orifice is consistent with the usual cosine law expected for excitations travelling similarly to rectilinear light:

$$\frac{W_{\rm p}}{W_{\rm BBR}} = c\left(\frac{r}{d_p}\right)^2 \cos^2\varphi_p. \qquad (2)$$

Here the ratio of $W_{\rm p}$ and $W_{\rm BBR}$ corresponds to the ratio of incident (detected) and emitted quasiparticle fluxes. The so-called "width parameters" $W_{\rm p}$ and $W_{\rm BBR}$ of the pixel and BBR source are proportional to the power deposited inside the pixel and BBR source [10]. These are inferred from damping of the tuning fork located inside the pixel's cavity ($W_{\rm p}$) and the damping of the thermometer wire inside the BBR ($W_{\rm BBR}$), see the Materials and Methods for details. In Eq. 2 r is the pixel radius, φ_p is the angle subtended by the centre of the face of pixel p to the normal of the radiator orifice and d_p is the distance between the centre of the pixel face and the radiator orifice. The geometrical coefficient c reflects the different power sensitivities of the BBR and camera pixels, and is less than unity due to the open geometry of the camera pixels.

Figure 3 presents the ratio of incident and emitted quasiparticle fluxes and compares our measurements to the analytical prediction and the result of numerical simulation. The central image shows red points corresponding to the experimental data measured by each pixel of the camera and a simulated profile of the beam. The horizontal plane below the numerical profile is a copy of inset image. The left and right panes of the figure illustrate projections of the profile by camera columns and rows, respectively. The solid curves on the panes corresponding to the peripheral rows 'A', 'E' and column '5' are analytically calculated using Eq. 2 with the constant c equal to 0.23. The situation with the inner pixels is more complicated, since a significant fraction of the incident quasiparticles may pass through a pixel cavity without scattering with its walls, or may scatter behind the sensitive part of the tuning fork detector and as a result will not contribute towards the fork's damping. Therefore the analytical expression for the power detected power at these pixels in Eq. 2, with a constant $c = 0.23$, overestimates the observed signal for these pixels and is not shown in Fig. 3.

We have attempted to allow for undetected quasiparticles using a numerical simulation. The simulation uses a point-source of quasiparticles with $\cos\varphi$ angular distribution placed in the centre of the BBR orifice, the dimensions of our cell and an assumption that incident quasiparticles contribute towards the measured signal if they scatter with the pixel's wall within a certain distance (identical for all the pixels) from the front face of the pixel. Further details are in the Materials and Methods section. The dashed curves in Fig. 3 plotted for all of the rows and columns are the results of the numerical simulation with quasiparticles contributing to the measured signal provided they scatter with the pixel wall within 1.4 mm of the pixel's opening. This value is in good agreement with our camera design, since the sensitive part of the tuning fork is on average about 1 mm below the camera face. Our observations also show that the measured beam profile remains constant with the variation of emitted power by nearly two orders of magnitude (from 20 pW to 800 pW). The good overall agreement between measurements, analytical expression and numerical simulations shows that ballistic quasiparticles emitted by the BBR source travel similarly to light and are suitable for imaging various topological objects that scatter quasiparticles, including turbulence.

C. Image of the Turbulent Tangle

At the lowest temperatures, the quasi-isotropic superfluid ^{3}He-B phase is stable and has a uniform energy gap, similar to conventional superconductivity in metals. In complete analogy to superconductors the ^{3}He-B quasiparticles experience Andreev reflections [28] and

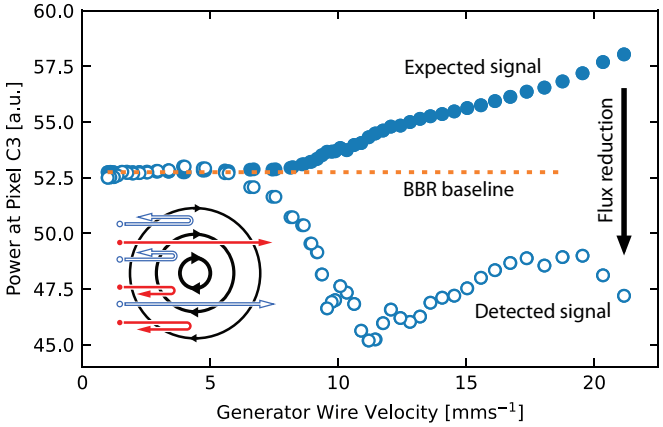

FIG. 4. The principle behind the measurement of turbulent shadow on camera pixel C3. The blue open circles show the power measured by pixel C3 as a function of the generator wire velocity. The orange dashed line equals the power detected by the pixel below the onset of pair-breaking and turbulence production on the generating wire and corresponds to the power emitted by the BBR. The blue solid circles is the sum of the BBR and generator beam powers expected to reach pixel C3 in the absence of vortices. The observed flux reduction is the signature of Andreev reflection and presence of turbulence (see text). The inset illustrates the Andreev reflection of quasiparticles (red solid circles) and holes (blue open circles) approaching the velocity flow field surrounding a quantum vortex (see text).

offer a means of mapping the contours of the order parameter, providing the access to static and dynamic processes which perturb it [29]. The inset of Fig. 4 sketches trajectories of quasiparticles (red solid arrow) and quasiholes (blue open arrow) approaching a quantised vortex and the result of interaction with superfluid flow field surrounding the vortex. Depending on the excitation energy, the distance to the vortex core and the direction of the flow quasiparticles and quasiholes may pass or be Andreev (retro-) reflected and retrace their incoming path [32]. While the vortex core is on the order of the coherence length (∼100 nm), the characteristic cross-section length scale for Andreev reflection is macroscopic and at temperature of 150 µK is 4.2 µm [33]. Thus in the presence of quantised vortices a fraction of the illuminating beam of quasiparticles is Andreev retro-reflected, and produces a shadow behind the vortex [34].

To detect turbulence we operate the BBR in a "furnace" mode with its beam of quasiparticles directed towards the generator wire and camera. If the generator wire does not produce vortices a combined flux of quasiparticles emitted by the generator and BBR should reach the camera. The method of determining the turbulent shadow is illustrated in the Fig. 4 using data of camera pixel C3. The empty blue circles correspond to the actual, measured data of pixel C3 and are labelled "Detected Signal". At low generator velocities, below onset of pair-breaking, the pixel's response is constant as it detects only the quasiparticles emitted by the BBR in a "furnace" mode. We use this data as a baseline and draw an orange dashed line labelled "BBR baseline" towards higher velocities. In the absence of turbulence, the pixel should detect the combined quasiparticle flux of the BBR ("Baseline") and generator wire (data of pixel C3 from Fig. 2), which we plot using filled blue circles and label "Expected Signal". The measured data shows a reduction of the detected power at approximately 7.5 mm s^{-1} and is a signature of Andreev reflection by the vortices surrounding the wire. It is convenient to characterise the local strength of the turbulent shadow via the fractional reduction in the flux of excitations incident on each pixel [32, 35]. Fractional screening is defined as the ratio of the difference between expected and measured fluxes and the expected flux emitted by the BBR and generator wire [16].

The right panel of Fig. 5 presents the fractional screening detected by diagonal pixels of the camera for generator wire velocities between 1 mm s^{-1} and 21 mm s^{-1}. The detailed distribution of the turbulent shadow is best illustrated by the snapshots of the camera at four different velocities on the left panel of Fig. 5. We can immediately see various features of interest. (i) The onset of turbulence appears at a velocity of about 7 mm s^{-1}, in the vicinity of pair-breaking as shown in Fig. 1. The turbulence accompanying onset of pair-breaking is consistent with the previous measurements using oscillatory wires in ^{3}He-B [36]. (ii) Above that velocity, the fractional screening for the majority of camera pixels grows steadily until the generator velocity reaches ≈ 12 mm s^{-1} and reflects a gradual increase in the density of the turbulent tangle with increasing velocity. (iii) The Hinton-based diagrams on the left panel of Fig. 5 demonstrate a significant difference between the top and bottom of the shadowgram, with the majority of the shadowing arising in the centre and top of the camera pixels (above the generator wire). It is clear that the turbulence distribution is strikingly different from almost symmetrical quasiparticle beams emitted from the BBR and generator wire.

III. MECHANISM OF TURBULENCE PRODUCTION IN ^{3}HE-B

Our setup measures the integral amount of vortices on a direct line of sight between the quasiparticle source and the camera. Figure 6 shows the most probable configuration of a vortex tangle surrounding the generator wire, which results in the absence of turbulence below the wire. Previously, several experiments [26, 37] and simulations [20, 37–39] have observed differences in the turbulent tangle production in the directions parallel and perpendicular to the oscillating object's path. In our experiment the reported tangle configurations (Fig. 6 inset A and B) will result in a symmetrical shadow. In the simulations of Ref. [38] the vortex line density around the oscillating sphere shows bifurcation: a tangle has shown a tendency to form more strongly on one side

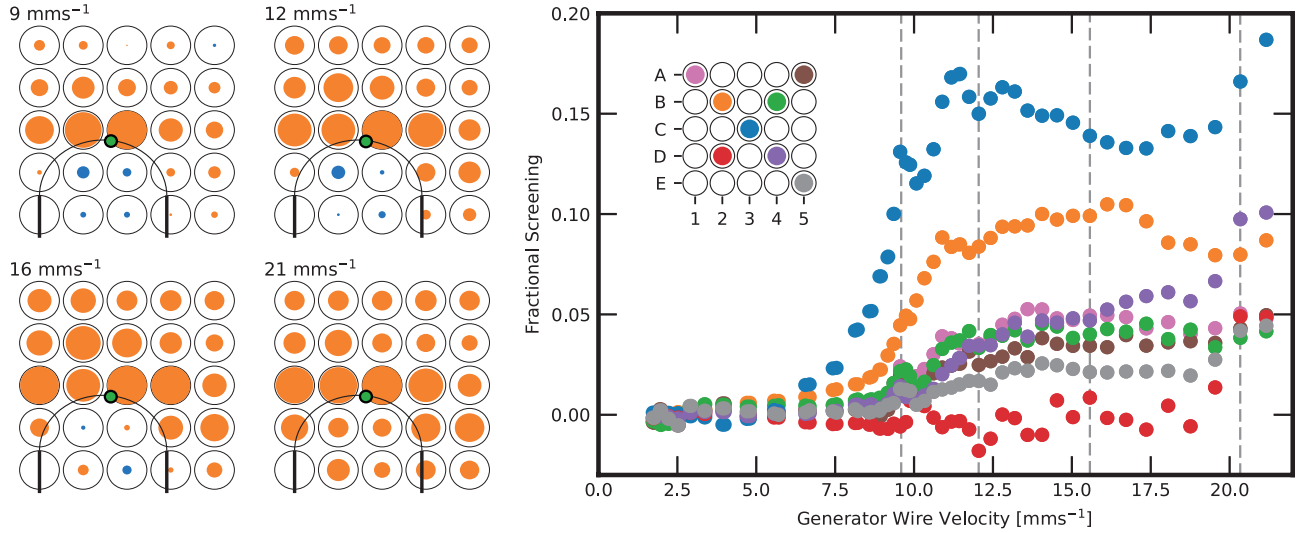

FIG. 5. "Shadowgram" of a turbulent tangle produced by the generator wire and illuminated by the blackbody radiator quasiparticle source. *(Left)* Hinton-based diagrams of the detected turbulence for four generator wire velocities that are marked on the left panel of this figure as the dashed vertical lines. The orange and blue colors correspond to positive and negative values, respectively. All the diagrams are normalised by the same value of fractional screening. The measured turbulent shadow differs drastically from the quasiparticle beams and indicates that vortex production is highly non-uniform around the wire. The green circle shows the scaled size and location of the BBR orifice. *(Right)* The dependence of fractional screening (amount of turbulence) for the diagonal pixels of the camera as a function of the generator wire's velocity. The camera detects vortices when the generator wire reaches the onset velocities for pair-breaking. The turbulent screening increases until a velocity of $12\,\mathrm{mm\,s^{-1}}$ and then remains nearly constant.

of an oscillating sphere independently of the particular form of seed vortex. Inset A of Fig. 6 illustrates that such tangle configuration occurring in front of a cylindrical oscillator is symmetrical with respect to the illuminating beam. Similarly, inset B on Fig. 6 depicts a tangle developing stronger in the direction perpendicular to the wire's motion, which has been inferred in vibrating wire experiments in ^{4}He [26] and successfully simulated by colliding two vortex-ring fronts traveling in the direction of wire's motion [20]. Our experiment suggests that in superfluid ^{3}He nucleated vortices survive predominately on the top of the semicircular generator wire and an endless succession of shedding off vortex loops ("vortex mill") [20, 22, 23] is not operating around the whole periphery of the wire.

Let us address nucleation processes first. In superfluid ^{4}He, a tangle often develops from remnant vortices, which include vortices formed during the superfluid transition [37, 40]. Superfluid ^{3}He prefers nucleation of vortex lines via intrinsic processes [40, 41] due to the three orders of magnitude lower value of Landau's critical velocity and correspondingly large vortex core [1]. Conceptually, the intrinsic nucleation in the vicinity of critical velocity can be understood as a flow near a surface leading to an instability of the normal component and subsequent production of a vortex line due to the mass conservation [3, 8, 42]. Experiments in ^{3}He-B have demonstrated that the critical velocity for intrinsic vortex creation at a surface falls with the increasing roughness of the boundary [42]. Additionally, due to a large cross-section of a

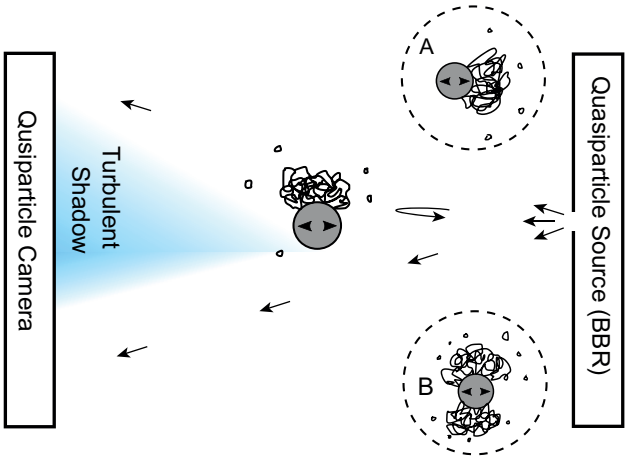

FIG. 6. A side-on sketch of the experiment with the most probable tangle configuration (not to scale). We illuminate the turbulence created by the wire with a quasiparticle flux emitted from the orifice of the blackbody radiator. A fraction of quasiparticles experience Andreev retro-reflection, and retrace their path leaving a shadow behind the vortex tangle. The quasiparticle camera detects the reduction of flux and 'images' distribution of quantum turbulence formed by the wire. The insets A and B show tangle distribution resulting in symmetrical shadow: in (A) turbulence forms behind the wire's direction of motion, while in (B) turbulence develops above and below the wire.

neutron capture in ^{3}He, it is possible to nucleate vortices via the Kibble-Zurek mechanism when cosmic rays travel through the cell [43]. Provided the capture and energy release take place in the vicinity of a moving generator wire the created vortex loops may be trapped on the wire surface. Our BBR when operated in the detector mode at 110 µK observes approximately one such capture event per minute in its $4\times4\times4\,\mathrm{mm}^3$ volume and the probability of an event to take place near the moving apex of a wire ($10\,\mu\mathrm{m}\times10\,\mu\mathrm{m}\times1\,\mathrm{mm}$) is approximately a million times smaller. Regardless of the exact nature of the vortex nucleation model, intrinsic or extrinsic, for an ideal cylindrical wire one expects nearly identical emission of vortex rings above or below the generation wire.

It is tempting to attribute the difference in the turbulence production to an excess of excrescences present on the top of the wire. Recent numerical simulations of quantum turbulence in ^{4}He demonstrate the importance of "peaks" on the surface where the superfluid flow is enhanced and produces localised vortices [25]. Such excrescences enhance the local superfluid velocity in ^{3}He as well and should aid in the vortex production. The actual distribution of such nucleation and pinning centres on the generator wire's surface is unknown and it is unclear why they would predominantly appear on the top of the wire. Furthermore, the large vortex core in superfluid ^{3}He makes vortex pinning unlikely. The excrescences have to be significantly larger than the vortex core size (100 nm) to pin vortices, and smaller than the wire diameter of 4.5 µm. The critical velocity for unpinning a vortex loop filament with a diameter of 10 µm on pinning asperities with sizes of 300 nm is $1.4\,\mathrm{mm\,s^{-1}}$ [44, 45], which is significantly smaller than measured turbulence onset velocity. Thus excrescences cannot explain the turbulence asymmetry in ^{3}He.

The vortex loops present at the wire surface expand under the influence of the superflow relative to the wire. An applied ac flow buckles a pinned vortex until it eventually reconnects with itself and emits a vortex ring. The "vortex mill" is thought to be particularly efficient when the frequency of the oscillating flow matches the first Kelvin wave resonance of the pinned vortex [22]. In such a process the emitted rings have a diameter comparable to the initial length of the vortex line [23]. For our generator wire oscillating at 354 Hz, the emitted rings should have a diameter of 7.1 µm. The onset velocity for the ring emission is expected to be similar to the self-induced velocity of the produced rings [23]. In superfluid ^{3}He, the 7.1 µm vortex rings have a velocity of $7.9\,\mathrm{mm\,s^{-1}}$ [22] and thus the onset velocity is almost identical to the third of Landau critical velocity.

Asymmetry could also be attributed to the existence of bridge vortices that stretch from the generator wire towards the top walls of the experimental cell, camera or BBR [38, 46], and are produced while passing the superfluid transition. However, the reproducibility of turbulence shadow between measurements including thermally cycling the cryostat to room temperature makes this scenario unlikely. The polarity of the trapped vortices as well can not explain the shadow asymmetry since the ac flow changes the direction every half cycle and would result in alternative direction of the emitted vortex loops.

Our results show that a turbulent shadow developed above the wire is substantial and hence we assume that a vortex mill is operating on the top surface of a semicircular wire. The inability to sustain a vortex production below the wire has to come from the curvature of the generator wire and we conclude that the vortex loops are more stable on the top and disappear from the lower part of the wire. Traditionally investigations into the stability of vortices on a surface are carried out by considering image vortex methods [44, 47]. Presently, we are unaware of theoretical works or numerical simulations of vortex dynamics on a cylindrical surface with dimensions comparable to the vortex core and hope that the results of our experiments will inspire such efforts.

Figure 5 shows that near a velocity of $12\,\mathrm{mm\,s^{-1}}$ the turbulent shadow stops growing and becomes more uniform. We attribute the behaviour change of the shadow to the ability of the moving wire and attached vortex lines to retrap the escaping rings. The distance travelled by emitted vortex rings with a diameter of 7.1 µm during a quarter cycle of the wire is about 5.6 µm, which matches the generator wire displacement of 5.4 µm at its velocity of $12\,\mathrm{mm\,s^{-1}}$. Retrapping vortex rings will create a tangle surrounding the whole wire and should produce a more uniform turbulent tangle. While the tangle should become denser in the vicinity of the wire, it does not always translate into stronger shadow as overall flow fields around non-polarised vortices can be cancelling each other. Previous measurements of grid turbulence [17] and numerical simulations [34, 48] have shown that morphological transformation of vortex configuration from ballistic vortex rings to a tangle may not apparent in Andreev reflection, and time-of-flight measurements are required to clarify the vortex dynamics.

IV. CONCLUSIONS

We exploit the ballistic dynamics of quasiparticles in superfluid ^{3}He-B to develop quasiparticle imaging techniques. We use black body radiators operating in a "furnace" mode to construct a quasiparticle source and in a detector mode to build a 5×5 pixel quasiparticle camera. Using our setup we probe the appearance of pair-breaking and accompanying vortices. At lower velocities the turbulence distribution around the wire leads to the conclusion that vortex loops are more stable on top of the semicircular wire loop. At the highest generator wire velocities, the escaping vortex rings can be re-trapped and the turbulence distribution become more uniform.

The quasiparticle beam emitted by the blackbody radiator source has a constant profile regardless of the emitted power, is well described by the usual cosine law for a light emitting disk and thus validates further devel-

opment of quasiparticle cameras in superfluid ^{3}He. A next generation camera will utilise high-resolution sensors built from micro- and nano-electromechanical systems that are currently under development [49–52]. The use of these devices will open new areas of study such as detecting topological objects remaining after the collision of two superfluid A-B interfaces [53], and investigating the scattering of quasiparticles from surfaces [54, 55].

ACKNOWLEDGMENTS

We thank S. M. Holt, A. Stokes, and M. G. Ward for excellent technical support. This research was supported by the UK EPSRC Grants No. EP/L000016/1, No. EP/I028285/1 and the EU H2020 European Microkelvin Platform (grant agreement 824109).

Data Availability

All the data in this paper is available from the Lancaster University data repository: at XX.

Appendix A: Materials and methods

1. Cooling Techniques

To achieve the necessary low temperatures, we use a combination of a sub-2 mK dilution refrigerator [56] and the adiabatic nuclear demagnetization of copper plates in a Lancaster double-wall experimental cell [57]. The quasiparticle source, camera, and thermometer wires are placed at the centre of the inner cell, surrounded by the refrigerant plates, coated with silver sinter to provide thermal contact to the helium superfluid. The plates absorb the excess of quasiparticles after each experiment and can maintain temperatures below 150 µK for up to four days, depending on the level of heat generated during measurements. The typical starting conditions for a demagnetization run are a temperature of 5 mK, in a field of 6.3 T. To reach the microkelvin regime we then demagnetize to ∼30 mT. The small final field also provides the field B for operating the vibrating wires used for heating and thermometry [58].

2. Detector Operation

The VWRs are semi-circular superconducting NbTi wires with a leg spacing L. They are set into motion by the oscillating Laplace force $F = (\pi/4)BI_0L$ that is generated by an applied alternating current I_0. As the top of wire loop moves through the magnetic field with the velocity v a Faraday voltage $V = (\pi/4)BLv$ is induced across the wire [59, 60].

The camera's quartz tuning forks are operated by using their piezoelectric properties. An applied voltage V creates a force $F = (1/2)aV$ on the fork's prongs, where a is an experimentally determinable fork constant. The deformation then causes a piezo-current I directly proportional the prong's velocity v, $I = av$ [61].

A frequency sweep of each type of resonator allows us to find the resonance frequency, amplitude and width by fitting a Lorentzian peak to the data. After determining these values we can track the resonance during camera measurements allowing us to find the width (damping) of each resonator during an experimental run [30].

3. Detector Calibration

The damping felt by the cell detectors (VWRs and tuning forks) is strongly related to the quasiparticle flux and geometric constants unique to each device [62]. By measuring over a wide temperature range as the cell warms up different devices are calibrated by comparison to a previously calibrated VWR. This allows for sensitive thermometry and flux detection over the course of measurements.

4. Andreev Reflection

Quasiparticle excitations travel in the "vacuum" provided by the superfluid condensate and are sensitive to changes in the order parameter since, unlike a true vacuum, the superfluid condensate has its own inertial reference frame. In a superfluid flowing with velocity $\mathbf{v}$ the energy-momentum dispersion curve of quasiparticles $E(\mathbf{p})$ is tilted (by the $\mathbf{p_F} \cdot \mathbf{v}$ Galilean transformation, where $\mathbf{p_F}$ is the Fermi momentum) and this presents an effective potential to the quasiparticles [63]. Spatial variations in the energy gap (e.g. from textures in high fields or from phase interfaces) also result in a potential barrier for quasiparticles. If an excitation has insufficient energy to propagate through the potential barrier, then it is Andreev reflected [28]. Excitations can only exchange a very small momentum with the condensate, so Andreev reflection exerts very little force, whilst it changes the character of the excitation (particles to holes and vice versa) thus reversing their direction. Andreev "retro-reflection" of excitations therefore provides a very convenient, non-invasive mechanism for imaging order parameter variations and topological defects in the superfluid [29, 33].

5. The Width Parameter of the Black Body Radiator and camera

The "width parameter" [10], $W_\mathrm{p} = \Delta f_2^\mathrm{p} T \widetilde{E}$, is a measure of the quasiparticle flux (number of particles crossing a unit area per unit time), and is deduced from the width

of the mechanical resonance of the tuning fork located inside the pixel's cavity $\Delta f_2^{\rm p}$, the pixel's temperature T [58] and the average energy of quasiparticles $\widetilde{E} = k_{\rm B}T + \Delta$, where Δ is the superfluid energy gap. The pixel's temperature and average quasiparticle energies are obtained from the resonance width of the detector using prior calibrations. The width parameter is proportional to the power deposited in the pixel $\dot{Q}_{\rm p} = c_{\rm p} W_{\rm p}$, where $c_{\rm p}$ is the constant of proportionality [10]. The similar constant for the BBR, $c_{\rm B} = \dot{Q}_{\rm B}/W_{\rm B}$, linking the deposited power $\dot{Q}_{\rm B}$ and the width parameter of the BBR, $W_{\rm B} = \Delta f_2^{\rm B} T \widetilde{E}$, can be measured from a known power using the BBR heater and the resonance width of the BBR thermometer $\Delta f_2^{\rm B}$ [10]. To calibrate the BBR we operate it in the "furnace" mode and apply a known power $\dot{Q}_{\rm B} = Fv$ to the BBR heater, where F is the force and v is the velocity of the heater wire. In the equilibrium state, determined by reaching a constant temperature inside the BBR, the emitted quasiparticle flux must carry away all the power deposited in the BBR box. The left panel of Fig. 2 shows the detected power in arbitrary units, since the camera pixels do not permit direct calibration in "furnace" mode due to absence of an independent thermometer. Hence, the actual power is proportional to this number but relies on geometric arguments. While the calibration for a camera pixel $c_{\rm p}$, is not available directly, it is constant and we can study the ratio of detected ($\dot{Q}_{\rm p}$) and emitted ($\dot{Q}_{\rm B}$) powers using the measured width parameters (see Eq. A2). Figure 3 plots the ratio of the width parameters.

6. Angular Distribution of BBR Emitted Quasiparticles

Our camera allows us to determine the angular distribution of the emitted quasiparticle beam by analysing the fraction of quasiparticles received by every pixel. For an ideal BBR, the power carried by ballistic quasiparticles escaping the BBR orifice should be consistent with the usual cosine law expected for light rays emitted by a disk. The fraction of quasiparticle flux received by a central pixel of the camera can be estimated by placing a source at the centre of a sphere and following steps for the derivation of the surface area of a cap with radius r for a sphere with radius R and normalizing it to the area of half of a sphere. Taking the elementary area of a sphere surface to be $dA = R^2 d\theta \sin\phi \, d\phi$, where $\theta = (0, 2\pi)$ is the azimuthal angle, and $\phi = (0, \pi/2)$ is the inclination (polar) angle we add a $\cos\phi$ dependence to account for the reduction of the effective area of a disk (BBR's orifice) when the emission direction differs from the disk normal. The resulting fraction of power (quasiparticle flux) emitted towards a central pixel becomes:

$$\frac{\dot{Q}_{\rm cen}}{\dot{Q}_{\rm B}} = \frac{1}{\pi} \int_0^{2\pi} d\theta \int_0^{\arcsin\left(\frac{r}{R}\right)} \cos\phi \sin\phi \, d\phi = \left(\frac{r}{R}\right)^2 \quad \text{(A1)}$$

For a non-central pixel p of the camera with a radius r the expected fraction of quasiparticles is:

$$\frac{\dot{Q}_{\rm p}}{\dot{Q}_{\rm B}} = \frac{c_{\rm p} W_{\rm p}}{c_{\rm B} W_{\rm B}} = \left(\frac{r}{d_p}\right)^2 \cos^2\phi_p = \left(\frac{r}{R}\right)^2 \cos^4\phi_p, \quad \text{(A2)}$$

where d_p is the distance from the center of the pixel face to the radiator orifice, ϕ_p is the angle subtended by the center of the pixel face and R is the distance between the BBR source and the camera. The ratio $c_{\rm p}/c_{\rm B}$ accounts for the different power sensitivities of the BBR and a camera pixel and is expected to be less than unity because of the much more open geometry of the camera pixels.

Clearly it is a straightforward geometrical exercise to calculate the flux of excitations from the source entering the front of each pixel, as expressed in Eqs. A1 and A2. However, the quasiparticles entering the pixels must then hit the pixel's cavity boundaries to create the "equilibrium" excitation gas inside a pixel that is probed by the tuning fork. For complex reasons tuning forks are only sensitive to thermal distributions. Since, as mentioned above, this conversion is not accessible to measurement, we need to calibrate the pixels using the expression (above) $\dot{Q}_{\rm p} = c_{\rm p} W_{\rm p}$ to find the power deposited in each pixel from the pixel width parameter. This is straightforwardly done for the peripheral pixels, where the incoming quasiparticles are travelling at a large angle to the cavity axis and all will strike a cavity surface. The comparison of the calculated incident quasiparticle flux and the signal measured by the fork for the peripheral cavities provides the calibration, i.e. it fixes the constant c_p above.

For the central pixels not all the incident quasiparticles impinge on an inside wall, and some are able to pass straight through. It is cumbersome to take this into account with an analytical expression, i.e. by adding a correction to Eqs. A1 and A2 above and we have instead simulated the behaviour by an essentially Monte Carlo method, ray tracing quasiparticle trajectories through the pixel cavities. The simulation uses 10^6 quasiparticles uniformly distributed on the location of BBR orifice, the actual dimensions of our cell and the same constant c_p for all camera pixels. We also assume that incident quasiparticles contribute towards the measured signal if they scatter with the pixel's wall within a certain distance from the front face of the camera, which is identical for all the pixels. Result of this calculation corresponds to the three-dimensional surface illustrated in Fig. 3 along with the dashed lines on the side panels. As can be seen, the agreement with the measured data is rather good given the complex geometry of the system.

[1] C. Enns and S. Hunklinger, *Low-Temperature Physics* (Springer-Verlag Berlin Heidelberg, 2005).

[2] D. I. Bradley, S. N. Fisher, A. M. Guénault, R. P. Haley, C. R. Lawson, G. R. Pickett, R. Schanen, M. Skyba, V. Tsepelin, and D. E. Zmeev, Breaking the superfluid speed limit in a fermionic condensate, Nat. Phys. **12**, 1017 (2016).

[3] J. A. Kuorelahti, S. M. Laine, and E. V. Thuneberg, Models for supercritical motion in a superfluid Fermi liquid, Phys. Rev. B **98**, 144512 (2018).

[4] S. Autti, J. T. Mäkinen, J. Rysti, G. E. Volovik, V. V. Zavjalov, and V. B. Eltsov, Exceeding the Landau speed limit with topological Bogoliubov Fermi surfaces, Phys. Rev. Research **2**, 033013 (2020).

[5] D. Vollhardt and P. Wölfle, *The Superfluid Phases of Helium 3* (Taylor and Francis, 1990).

[6] R. Dobbs, *Helium Three* (Oxford University Press, 2001).

[7] G. E. Volovik, Topological invariant for superfluid ^{3}He-B and quantum phase transitions, JETP Lett. **90**, 587 (2009).

[8] A. Calogeracos and G. E. Volovik, Critical velocity in ^{3}He-B vibrating wire experiments as analog of vacuum instability in a slowly oscillating electric field, J. Exp. Theor. Phys. **88**, 40 (1999).

[9] G. E. Volovik, Fermion zero modes at the boundary of superfluid ^{3}He-B, JETP Lett. **90**, 398 (2009).

[10] S. N. Fisher, A. M. Guénault, C. J. Kennedy, and G. R. Pickett, Blackbody source and detector of ballistic quasiparticles in ^{3}He-B: Emission angle from a wire moving at supercritical velocity, Phys. Rev. Lett. **69**, 1073 (1992).

[11] C. J. Lambert, Theory of pair breaking by vibrating macroscopic objects in superfluid ^{3}He, Physica B: Condens. Matter **178**, 294 (1992).

[12] R. Blaauwgeers, V. B. Eltsov, M. Krusius, J. J. Ruohio, R. Schanen, and G. E. Volovik, Double-quantum vortex in superfluid ^{3}He-A, Nature **404**, 471 (2000).

[13] S. Autti, V. V. Dmitriev, J. T. Mäkinen, A. A. Soldatov, G. E. Volovik, A. N. Yudin, V. V. Zavjalov, and V. B. Eltsov, Observation of Half-Quantum Vortices in Topological Superfluid ^{3}He, Phys. Rev. Lett. **117**, 255301 (2016).

[14] S. N. Fisher and G. R. Pickett, Quantum turbulence, Phys. World **19**, 22 (2006).

[15] A. P. Finne, T. Araki, R. Blaauwgeers, V. B. Eltsov, N. B. Kopnin, M. Krusius, L. Skrbek, M. Tsubota, and G. E. Volovik, An intrinsic velocity-independent criterion for superfluid turbulence, Nature **424**, 1022 (2003).

[16] S. N. Fisher, A. J. Hale, A. M. Guénault, and G. R. Pickett, Generation and Detection of Quantum Turbulence in Superfluid ^{3}He-B, Phys. Rev. Lett. **86**, 244 (2001).

[17] D. I. Bradley, D. O. Clubb, S. N. Fisher, A. M. Guénault, R. P. Haley, C. J. Matthews, G. R. Pickett, V. Tsepelin, and K. Zaki, Emission of Discrete Vortex Rings by a Vibrating Grid In Superfluid ^{3}He-B: A Precursor to Quantum Turbulence, Phys. Rev. Lett. **95**, 035302 (2005).

[18] E. A. L. Henn, J. A. Seman, G. Roati, K. M. F. Magalhães, and V. S. Bagnato, Emergence of turbulence in an oscillating Bose-Einstein condensate, Phys. Rev. Lett. **103**, 045301 (2009).

[19] L. Skrbek, D. Schmoranzer, Š. Midlik, and K. R. Sreenivasan, Phenomenology of quantum turbulence in superfluid helium, Proc. Natl. Acad. Sci. U.S.A **118**, 10.1073/pnas.2018406118 (2021).

[20] T. Nakagawa, S. Inui, M. Tsubota, and H. Yano, Statistical laws and self-similarity of vortex rings emitted from a localized vortex tangle in superfluid ^{4}He, Phys. Rev. B **101**, 184515 (2020).

[21] V. Eltsov, R. Hänninen, and M. Kruius, Quantum turbulence in superfluids with wall-clamped normal component, Proc. Natl. Acad. Sci. U.S.A **111**, 4711 (2014).

[22] R. J. Donnelly, *Quantized Vortices in Helium II*, Vol. 2 (Cambridge University Press, 1991).

[23] R. Hänninen, A. Mitani, and M. Tsubota, Simple Pinning Model for Vibrating Wire Turbulence in Superfluid Helium at Zero Temperature, in *AIP Conf. Proc.*, Vol. 850 (2006) pp. 217–218.

[24] S. Fujiyama, A. Mitani, M. Tsubota, D. I. Bradley, S. N. Fisher, A. M. Guénault, R. P. Haley, G. R. Pickett, and V. Tsepelin, Generation, evolution, and decay of pure quantum turbulence: A full Biot-Savart simulation, Phys. Rev. B **81**, 180512(R) (2010).

[25] G. W. Stagg, N. G. Parker, and C. F. Barenghi, Superfluid boundary layer, Phys. Rev. Lett. **118**, 135301 (2017).

[26] H. Yano, K. Ogawa, Y. Chiba, K. Obara, and O. Ishikawa, Anisotropic Formation of Quantum Turbulence Generated by a Vibrating Wire in Superfluid ^{4}He, J. Low Temp. Phys. **187**, 515 (2017).

[27] P. M. Walmsley and A. I. Golov, Quantum and Quasiclassical Types of Superfluid Turbulence, Phys. Rev. Lett. **100**, 10.1103/PhysRevLett.100.245301 (2008).

[28] A. F. Andreev, The Thermal Conductivity of the Intermediate State in Superconductors, J. Exp. Theor. Phys **19**, 1228 (1964).

[29] D. Bradley, A. Guénault, R. Haley, G. Pickett, and V. Tsepelin, Andreev Reflection in Superfluid ^{3}He: A Probe for Quantum Turbulence, Annu. Rev. Condens. Matter Phys. **8**, 407 (2017).

[30] S. L. Ahlstrom, D. I. Bradley, S. N. Fisher, A. M. Guénault, E. A. Guise, R. P. Haley, S. Holt, O. Kolosov, P. V. E. McClintock, G. R. Pickett, M. Poole, R. Schanen, V. Tsepelin, and A. J. Woods, A Quasiparticle Detector for Imaging Quantum Turbulence in Superfluid ^{3}He-B, J. Low Temp. Phys. **175**, 725 (2014).

[31] S. Fisher, A. Guénault, C. Kennedy, and G. Pickett, Beyond the two-fluid model: Transition from linear behavior to a velocity-independent force on a moving object in ^{3}He-B, Phys. Rev. Lett. **63**, 2566 (1989).

[32] D. I. Bradley, S. N. Fisher, A. M. Guénault, M. R. Lowe, G. R. Pickett, A. Rahm, and R. C. V. Whitehead, Quantum Turbulence in Superfluid ^{3}He Illuminated by a Beam of Quasiparticle Excitations, Phys. Rev. Lett. **93**, 235302 (2004).

[33] S. N. Fisher, M. J. Jackson, Y. A. Sergeev, and V. Tsepelin, Andreev reflection, a tool to investigate vortex dynamics and quantum turbulence in ^{3}He-B, Proc. Natl. Acad. Sci. U.S.A **111**, 4659 (2014).

[34] V. Tsepelin, A. W. Baggaley, Y. A. Sergeev, C. F. Barenghi, S. N. Fisher, G. R. Pickett, M. J. Jackson, and N. Suramlishvili, Visualization of quantum turbulence in superfluid ^{3}He-B: Combined numerical and experimental study of Andreev reflection, Phys. Rev. B **96**, 054510

(2017).
[35] M. J. Jackson, D. I. Bradley, A. M. Guénault, R. P. Haley, G. R. Pickett, and V. Tsepelin, Observation of quantum turbulence in superfluid ^{3}He using reflection and transmission of ballistic thermal excitations, Phys. Rev. B **95**, 094518 (2017).
[36] D. I. Bradley, M. J. Fear, S. N. Fisher, A. M. Guénault, R. P. Haley, C. R. Lawson, G. R. Pickett, R. Schanen, and V. Tsepelin, Anomalous Damping of a Low Frequency Vibrating Wire in Superfluid ^{3}He-B due to Vortex Shielding, J. Low Temp. Phys. **175**, 372 (2014).
[37] R. Goto, S. Fujiyama, H. Yano, Y. Nago, N. Hashimoto, K. Obara, O. Ishikawa, M. Tsubota, and T. Hata, Turbulence in Boundary Flow of Superfluid ^{4}He Triggered by Free Vortex Rings, Phys. Rev. Lett **100**, 045301 (2008).
[38] R. Hänninen, M. Tsubota, and W. F. Vinen, Generation of turbulence by oscillating structures in superfluid helium at very low temperatures, Phys. Rev. B **75**, 064502 (2007).
[39] A. Nakatsuji, M. Tsubota, and H. Yano, Statistics of vortex loops emitted from quantum turbulence driven by an oscillating sphere, Phys. Rev. B **89**, 174520 (2014).
[40] W. F. Vinen and L. Skrbek, Quantum turbulence generated by oscillating structures, Proc. Natl. Acad. Sci. U.S.A **111**, 4699–4706 (2014).
[41] V. M. H. Ruutu, Ü. Parts, J. H. Koivuniemi, N. B. Kopnin, and M. Krusius, Intrinsic and Extrinsic Mechanisms of Vortex Formation in Superfluid ^{3}He-B, J. Low Temp. Phys. **107**, 93 (1997).
[42] Ü. Parts, V. M. H. Ruutu, J. H. Koivuniemi, Yu. M. Bunkov, V. V. Dmitriev, M. Fogelström, M. Huebner, Y. Kondo, N. B. Kopnin, J. S. Korhonen, M. Krusius, O. V. Lounasmaa, P. I. Soininen, and G. E. Volovik, Single-vortex nucleation in rotating superfluid ^{3}He-B, EPL **31**, 449 (1995).
[43] V. M. H. Ruutu, V. B. Eltsov, A. J. Gill, T. W. B. Kibble, M. Krusius, Y. G. Makhlin, B. Placais, G. E. Volovik, and W. Xu, Vortex formation in neutron-irradiated superfluid ^{3}He as an analogue of cosmological defect formation, Nature **382**, 334 (1996).
[44] K. W. Schwarz, Vortex Pinning in Superfluid Helium, Phys. Rev. Lett **47**, 251 (1981).
[45] K. W. Schwarz, Three-dimensional vortex dynamics in superfluid ^{4}He: Line-line and line-boundary interactions, Phys. Rev. B **31**, 5782 (1985).
[46] H. Yano, Y. Nago, R. Goto, K. Obara, O. Ishikawa, and T. Hata, Critical behavior of steady quantum turbulence generated by oscillating structures in superfluid ^{4}He, Phys. Rev. B **81**, 220507(R) (2010).
[47] W. I. Glaberson and R. J. Donnelly, Growth of Pinned Quantized Vortex Lines in Helium II, Phys. Rev **141**, 208 (1966).
[48] A. W. Baggaley, V. Tsepelin, C. F. Barenghi, S. N. Fisher, G. R. Pickett, Y. A. Sergeev, and N. Suramlishvili, Visualizing pure quantum turbulence in superfluid ^{3}He: Andreev reflection and its spectral properties, Phys. Rev. Lett **115**, 015302 (2015).
[49] M. Defoort, S. Dufresnes, S. L. Ahlstrom, D. I. Bradley, R. P. Haley, A. M. Guénault, E. A. Guise, G. R. Pickett, M. Poole, A. J. Woods, V. Tsepelin, S. N. Fisher, H. Godfrin, and E. Collin, Probing Bogoliubov Quasiparticles in Superfluid ^{3}He with a 'Vibrating-Wire Like' MEMS Device, J. Low Temp. Phys. **183**, 284 (2016).
[50] P. Zheng, W. G. Jiang, C. S. Barquist, Y. Lee, and H. B. Chan, Critical Velocity in the Presence of Surface Bound States in Superfluid ^{3}He-B, Phys. Rev. Lett. **118**, 065301 (2017).
[51] D. I. Bradley, R. George, A. M. Guénault, R. P. Haley, S. Kafanov, M. T. Noble, Y. A. Pashkin, G. R. Pickett, M. Poole, J. R. Prance, M. Sarsby, R. Schanen, V. Tsepelin, T. Wilcox, and D. E. Zmeev, Operating Nanobeams in a Quantum Fluid, Sci. Rep. **7**, 4876 (2017).
[52] T. Kamppinen and V. B. Eltsov, Nanomechanical Resonators for Cryogenic Research, J. Low Temp. Phys. **196**, 283 (2019).
[53] D. I. Bradley, S. N. Fisher, A. M. Guénault, R. P. Haley, J. Kopu, H. Martin, G. R. Pickett, J. E. Roberts, and V. Tsepelin, Relic topological defects from brane annihilation simulated in superfluid ^{3}He, Nat. Phys. **4**, 46 (2008).
[54] T. Okuda, H. Ikegami, H. Akimoto, and H. Ishimoto, Direct Observation of Quantum Andreev Reflection at Free Surface of Superfluid ^{3}He, Phys. Rev. Lett. **80**, 2857 (1998).
[55] Y. Nagato, M. Yamamoto, and K. Nagai, Rough surface effects on the p-wave Fermi superfluids, J. Low Temp. Phys. **110**, 1135 (1998).
[56] D. J. Cousins, S. N. Fisher, A. M. Guénault, R. P. Haley, I. E. Miller, G. R. Pickett, G. N. Plenderleith, P. Skyba, P. Y. A. Thibault, and M. G. Ward, An advanced dilution refrigerator designed for the new Lancaster microkelvin facility, J. Low Temp. Phys. **114**, 547 (1999).
[57] G. R. Pickett and S. N. Fisher, Superfluid ^{3}He in the zero-temperature limit, Physica B: Condens. Matter **329**, 75 (2003).
[58] C. Bäuerle, Yu. M. Bunkov, S. N. Fisher, and H. Godfrin, Temperature scale and heat capacity of superfluid ^{3}He-B in the 100 µK range, Phys. Rev. B **57**, 14381 (1998).
[59] D. I. Bradley, S. N. Fisher, A. M. Guénault, R. P. Haley, V. Tsepelin, G. R. Pickett, and K. L. Zaki, The transition to turbulent drag for a cylinder oscillating in superfluid ^{4}He: A comparison of quantum and classical behavior, J. Low Temp. Phys. **154**, 97 (2009).
[60] D. Schmoranzer, M. J. Jackson, Š. Midlik, M. Skyba, J. Bahyl, T. Skokánková, V. Tsepelin, and L. Skrbek, Dynamical similarity and instabilities in high-Stokes-number oscillatory flows of superfluid helium, Phys. Rev. B **99**, 054511 (2019).
[61] R. Blaauwgeers, M. Blazkova, M. Človečko, V. B. Eltsov, R. de Graaf, J. Hosio, M. Krusius, D. Schmoranzer, W. Schoepe, L. Skrbek, P. Skyba, R. E. Solntsev, and D. E. Zmeev, Quartz Tuning Fork: Thermometer, Pressure- and Viscometer for Helium Liquids, J. Low Temp. Phys. **146**, 537 (2007).
[62] D. I. Bradley, P. Crookston, S. N. Fisher, A. Ganshin, A. M. Guénault, R. P. Haley, M. J. Jackson, G. R. Pickett, R. Schanen, and V. Tsepelin, The Damping of a Quartz Tuning Fork in Superfluid ^{3}He-B at Low Temperatures, J. Low Temp. Phys. **157**, 476 (2009).
[63] S. N. Fisher, Turbulence Experiments in Superfluid ^{3}He at Very Low Temperatures, in *Vortices and Turbulence at Very Low Temperatures* (Springer, 2008) pp. 177–257.